



# An efficient detailed layer model for prediction of separator damage in a Li-Ion pouch cell exposed to transverse compression

Alexander Schmid<sup>a,\*</sup>, Christian Ellersdorfer<sup>a</sup>, Marco Raffler<sup>a</sup>, Nils Karajan<sup>b</sup>, Florian Feist<sup>a</sup>

<sup>a</sup> VSI - Vehicle Safety Institute, University of Technology Graz, 8010, Graz, Inffeldgasse 23/I, Austria

<sup>b</sup> DYNAmore FEM Ingenieurdienstleistungen GmbH, Industriestraße 2, 70565, Stuttgart, Germany

## HIGHLIGHTS

- Development of detailed modelling approaches of a lithium-ion cell.
- Focus on the computational efficiency of detailed modelling.
- Characterisation of cell components under transverse pressure.
- Determination of the mechanical behaviour of a cell under transverse pressure.
- Development of a short circuit prediction based on component failure.

## ARTICLE INFO

### Keywords:

Time efficient  
Detailed modelling  
Li-ion cell  
Separator  
ISC prediction  
Transverse compression

## ABSTRACT

Li-ion pouch cells can be understood as thin-layer laminates. Pressure loads normal to flat electrodes can cause failure or thermal runaway. However, detailed models for investigating transverse pressure loads in which each layer is resolved are computationally intensive. This paper outlines two approaches for time-efficient yet accurate detailed explicit finite element models of a cell. Both approaches are characterised by the fact that they are divided into in-plane and out-of-plane behaviour. The modelling of interlaminar contacts is completely omitted, to prevent parasitic contact compliance and efforts for contact handling. A discrete element formulation is used for a computationally efficient simulation of transverse loads. This prevents a reduction of the critical time step, which can result from transversal deformations. The difference between the two modelling approaches lies in the modelling of the out-of-plane behaviour. In the first approach, the behaviour in the out-of-plane direction is generated by characterising each component separately. The second approach assumes homogenous behaviour in the thickness direction. Both approaches rely on characterization data derived from component and cell tests. The cell models are validated against cell tests. Numerical results obtained with the two modelling approaches differ only slightly from the validation data.

## 1. Motivation and introduction

A damaged cell of a traction battery of electric vehicles can represent a significant hazard for all people involved in an accident [1]. To assess and – if necessary – avoid these situations, extensive knowledge of the crash behaviour of such vehicles and their electric energy storage systems (EESS) is required. The traction batteries of electric vehicles usually have a hierarchic design. A battery pack contains several modules. These, in turn, comprise individual cells [2]. Mechanical abuse and misuse can induce a thermal runaway [3]. In addition to electrochemical ([4–6]), electrical [7] and thermal aspects ([8–10]), the mechanical

behaviour ([11–13]) of the EESS, including safety assessment ([14–16]), is often the focus of attention. Liu et al. conducted an intensive study on the coupled mechanical-thermal-electrochemical (multi-physical) behaviour of lithium-ion cells and their modelling [17]. This multi-physical data can in turn be used to assess safety. For example, Xiao et al. used electrochemical impedance spectroscopy (EIS) measurements to diagnose internal cell damage [18]. Finegan et al. used the electrochemical and physical data to make predictions about safety using data-driven approaches [19]. Besides experiments [20], the tool of explicit simulation [21] is mainly used to evaluate the behaviour of lithium-ion cells.

\* Corresponding author.

E-mail address: [alexander.schmid@tugraz.at](mailto:alexander.schmid@tugraz.at) (A. Schmid).

<https://doi.org/10.1016/j.jpowsour.2023.233510>

Received 25 October 2022; Received in revised form 7 August 2023; Accepted 9 August 2023

Available online 12 August 2023

0378-7753/© 2023 The Authors. Published by Elsevier B.V. This is an open access article under the CC BY license (<http://creativecommons.org/licenses/by/4.0/>).

Common modelling approaches consider the cell to be a homogeneous structure, disregarding the heterogeneity of its constituents and providing advantages in terms of computational effort ([12–14,22–24]). This homogenisation allows larger element dimensions and fewer nodes and elements at the same time. Both have positive effects on computational efficiency. However, transferability is limited because characterisation tests are required again for each new cell model, as the models do not represent the individual component plies. For example, Beaumont et al. used three compression and two bending tests to calibrate a macroscopic model [24]. Although these modelling approaches can accurately replicate the behaviour of existing cells, they fall short of representing hypothetical cells under development without sufficient experimental data for calibration. To achieve transferability, it would be preferable to employ a model based on component properties. For a short-circuit criterion in homogenised models, numerous auxiliary parameters, such as strain [12,15] or stress ([22,25]) of selected elements are used. Raffler et al. used a strain-based failure criterion considering the axial and radial deformation of a cylindrical cell [12]. Xu et al. used a stress-state-based criterion, employing the unified strength theory (UST) [14]. The macroscopic modelling of a lithium-ion cell created by Trondl et al. uses neither a stress- nor a strain-based failure criterion. The relative volume is used to evaluate the internal short-circuit [26]. These types of criteria can be calibrated well but are only marginally related to the actual short-circuit cause, the separator failure.

RVE models examine a unit cell of the structure. This can be done to investigate micro-effects such as buckling [27]. Another use case is to generate homogenised material models from this ([15,28–32]). These are multi-scale approaches, as the cell is investigated on different length scales. Sahraei et al. used homogenisation theory to extract the mechanical behaviour of an RVE, including component failure [15]. These results are the basis for the macroscopic calibration of the cell model. For short-circuit prediction, a homogenised strain criterion is used. Jia et al. also determined the homogenised material behaviour of the RVE and linked this to a data-driven model to predict the safety risk [32]. Kermani et al. discussed buckling behaviour under in-plane loading at RVE and macroscopic levels [30]. The ability to generate cell behaviour from the behaviour of individual components is a major advantage over homogeneous approaches. Unfortunately, much information is lost due to the transfer from the RVE to the macroscopic scale, such as the deformation of individual components. Tang et al. used this multi-scale approach on the next scale. A representative section of the cell arrangement in the module is used to investigate the homogeneous behaviour of the module [29]. An approach that does not require diversion via several scale levels would be desirable. In addition, this should enable corresponding insight into the behaviour of individual subcomponents.

A physically detailed modelling approach enhances transferability because information about the constituents/plies suffices to construct a new cell model, thus potentially reducing the effort required for renewed characterisation tests. ([11,33–36]) Additionally, these models provide direct insight into the behaviour of individual parts. However, mesoscale models are computationally intensive, which rarely justifies their use for large-scale problems. In particular, the representation of the interactions between the individual components through contact modelling used by Breiffuss et al. drives up the computational effort [11]. A detailed modelling approach without contact between the individual components would be desirable, as this would contribute significantly to efficiency. The detailed modelling of the cell structure with subdivision of the electrodes into current collectors and active material often leads to smaller minimum dimensions of the elements. This is the case when the current collectors of the electrodes are thinner than the separators. Additionally, this leads to an increase in the number of elements and nodes. Both aspects negatively affect computational efficiency. The application of such subdivided approaches is justifiable at the RVE level. Modelling the entire cell is generally unnecessary, except for exceptional cases in which specific conditions apply. For

example, when load cases exhibit symmetries or when dimensional reduction from 3D to 2D is feasible. This would be the case, for example, with 3-point bending situations, which were investigated by Schaufelberger et al. [35]. Li et al. used 2D axisymmetric models in addition to 2D plane-strain models to keep the computational effort limited. In this work, the necessity of 3D full models was already emphasised, as they are suitable for all load conditions [36]. The disadvantage of these detailed 3D models is that they are connected with an enormous computational effort. Gilaki et al. refrained from mapping the interactions between individual components through contacts. This approach is used to model a 6P cylindrical cell through 22 million solid elements [33]. The model is used to simulate cell behaviour under radial loads. Applying this approach to pouch cells, an equivalent load (normal to the electrodes) would also lead to compression of the already thin layers. This would result in a reduction in the critical time step and, thus, an increase in the computational effort in an explicit simulation. In mesoscopic approaches, one often misses the prediction of the short-circuit [35]. Breiffuss et al. discussed the necessity and possible implementation. Extensive knowledge about the separator material is necessary to create a corresponding failure model. [11] Plaimer et al. conducted a detailed investigation of separator behaviour regarding electrochemical and mechanical performance. They showed the anisotropic behaviour of these plies [37]. Kalnaus et al. demonstrated that the behaviour of the separator is additionally dependent on the strain rate [38]. Xu et al. showed the influence of solvents in addition to anisotropy and strain rate influence. Thus, the tested samples behaved differently when dry or saturated with different fluids (water and DMC) [39]. Lagadec et al. conducted further studies on the performance and behaviour of the separator microstructure under mechanical loading ([40,41]).

A good compromise between the level of detail and computational efficiency in a lithium-ion cell model would be desirable. This would allow the implementation of a physics-based short-circuit criterion based on the state of the separator. Unfortunately, such well-balanced approaches are not yet described in the literature.

The authors address these issues in this paper. This work aims to combine the advantages of homogenised (time-efficiency) and meso-scale (physical accuracy) models by creating a computationally efficient layer-by-layer model of a cell. In this way, information on component behaviour does not have to be sacrificed for the sake of computational efficiency, as is the case with homogenised RVE approaches. In addition, it is not necessary to limit oneself to load cases that allow an application of 2D models (plane-strain or axisymmetric). The innovation of this work is the development of a modelling approach that combines the supposed opposites of computational efficiency and level of detail in an explicit FEM solver, subject to the regime of the Courant Criterion. The mesoscopic approach ensures the transferability of the model. The model allows for parameter studies related to the material and geometry of components. To balance the level of detail and computational efficiency the electrodes are not further divided into active materials and current collectors.

The Courant-Friedrichs-Levy (CFL) condition is a stability criterion for computing the critical admissible time step in a simulation using explicit time integration. This leads to increased computational effort in the case of thin plies modelled with solid elements. Subordinate approaches, such as shells or plates, are inapt when transverse loading is present. The situation is aggravated when external loads lead to further reduced element sizes and time steps. For a stable simulation, the time step must be sufficiently small to fulfil the CFL condition. This means that the time step must fall below a critical value (Equation (1)) [42].

$$\Delta t < \Delta t_{crit} \quad (1)$$

$$\Delta t_{crit} = \min_e(\Delta t_e) \quad (2)$$

The minimum time step of all elements  $e$  is used for the critical time

step  $\Delta t_{crit}$ . (Equation (2)) The element-related critical value  $\Delta t_e$  depends on the minimum element dimension  $l_{e\ min}$  and wave propagation speed  $c_e$ . (Equation (3))

$$\Delta t_e = \frac{l_{e\ min}}{c_e} \quad (3)$$

This also applies to the detailed modelling of lithium-ion cells under transverse loading. This work shows an approach that allows the simulation of the cell's transversal loads without deteriorating computational efficiency due to the compression of already thin layers.

The approach attempts to decrease simulation time as much as possible and therefore completely dispenses contact modelling between the component layers to find a good balance between detailed modelling and computational efficiency.

The separators are key players for cell failure. Two characteristic types of internal short-circuits can be distinguished [43]. Contact between the anode and cathode due to separator failure leads to a rapid drop in cell voltage (hard ISC). A gentle drop is caused by the flattening of the separator (soft ISC). This work focuses on predicting a hard ISC (rupture of the separator). An approach is presented in which the condition of these separators is used as a short-circuit criterion. For this purpose, a failure model for these components is implemented to generate a physics-based criterion and to avoid using auxiliary parameters.

## 2. Method

### 2.1. Cell under study

The cell used in this work is a nickel manganese cobalt (NMC) pouch cell with a mass of approximately 0.9 kg and a capacity of 41 Ah. The dimensions are  $260 \times 216 \times 7.8$  mm. The geometry and chemical composition of the components have been extensively examined by Kovachev et al. [44], and a summary of the key specifications of the single components is provided in Table 1. The cell features 85 layers in a pouch envelope. The 'jelly stack' comprises 42 separators, 21 cathodes and 22 anodes. Thickness was measured using the broad ion beam (BIB) cutting method.

The anodes' active material is graphite. This is applied to current collectors made of copper. The aluminium cathode current collectors are coated with LiNiMnCoO<sub>2</sub> (NMC). All current collectors have active material on both sides.

The separators comprise a 17  $\mu\text{m}$  thick structure made of polypropylene, covered with a 3  $\mu\text{m}$  of alumina (Al<sub>2</sub>O<sub>3</sub>). The enveloping pouch was identified as a composite of four layers. This comprises three layers of polymers and one layer of aluminium [44].

### 2.2. Modelling approach

The model was established in the explicit FEM solver LS-DYNA (R13 developer version (SVN 134893) for MPP double precision).

The meso-scale model of the pouch cell was established considering the following approaches, to reduce computational effort and

**Table 1**  
Dimensions of the components in the thickness direction [44].

Component	Thickness [ $\mu\text{m}$ ]	Number of plies	Material
Anode	140	22	
Anode CC	10	22	Copper
Anode AM	65	44	Graphite
<b>Cathode</b>	<b>170</b>	<b>21</b>	
Cathode CC	20	21	Aluminium
Cathode AM	75	42	NMC (LiNiMnCoO <sub>2</sub> )
<b>Separator</b>	<b>20</b>	<b>42</b>	Polypropylene
<b>Pouch</b>	<b>190</b>	<b>2</b>	Polymers and aluminium

AM: active material; CC: current collector.

simultaneously achieve numerical robustness:

- Separation into in-plane and out-of-plane behaviour,
- Combination of different sub-layers, like active materials and current collectors, to increase the critical time-step,
- Avoidance penalty or kinematic constraint contacts to simplify simulations and rule out potential contact instabilities or unwanted penetrations,
- Application of a discrete element formulation to rule out time-step drops due to massive element distortions in out-of-plane compression, and
- Implementation of a physical failure model for the separator plies.

For further discussion, a cell coordinate system is introduced, where the u-axis points towards the terminals, the w-axis is normal to the planar electrodes and the v-axis is perpendicular to the u- and w-directions (Fig. 4). In-plane loading (u- and v-axis) is handled by time-efficient shell elements, while out-of-plane loading and interlaminar shear are modelled by solid elements. As the in-plane behaviour is already covered by the corresponding shell elements, it is crucial for the solid elements to solely depict the out-of-plane transverse behaviour and shear. This requires a decoupled material model that generates no stresses upon u-, v- and uv-loading while providing response to w-, vw- and wu-loading. Two model variants are investigated (Fig. 1). In variant A, each component is defined separately regarding in-plane and transversal behaviour. The separator is modelled as a shell-solid-shell, while the anode and cathode are constructed as solid-shell-solid laminate. As the entire stack of components begins and ends with an anode, the enveloping pouch needs to be modelled in the same scheme as the separator layers.

In variant B, the individual components are modelled as shell elements only again depicting the in-plane behaviour only. The out-of-plane behaviour is depicted again by solid elements with homogenous characteristics over the entire cell thickness. Fig. 1 visually contrasts both approaches. In both variants, shell and solid elements alternate over thickness.

The intention of this hybrid modelling approach is to model the in-plane behaviour of the electrodes and separators via shell elements. Solid elements are used to represent the pressure deflection between the shells.

The structure of a Li-ion pouch cell is a stack of very thin plies comparable to a laminate. Accordingly, the dimension in the thickness direction is decisive for the time step of the explicit simulation. In variant A, the electrodes are not subdivided into current collectors and active materials. Considering Table 1, this induces an increase in the minimum element dimension because the thickness of the current conductors is smaller than that of the separators. With variant B, the minimum dimension is further increased. In addition, as homogenisation takes place in the w-direction, the minimum dimension of the solid elements is not limited to the thickness of the separators.

As the solid elements cover the interaction between the various plies through their shear behaviour, contact modelling is not necessary. Shell and solid elements constituting the individual plies share nodes.

The decoupled material model for solids is combined with a discrete element formulation. This formulation applies to materials with a Poisson's ratio equal to zero. The time step of an element  $\Delta t_e$  can also be calculated by the maximum natural frequency  $\omega_{max}$  (Equation (4)). The natural frequencies depend on the mass matrix  $M$  and stiffness matrix  $K$  (Equation (5)). The main difference to continuum-mechanical finite elements is that the stiffness matrix  $K$  is independent of the element length for discrete elements. Thus, the time step depends only on the element's mass and (maximum) stiffness. This is a great advantage in computational effort considering Equations (1)–(3). Therefore, no time-step drops are observed upon element distortion, e.g. due to transverse compression.

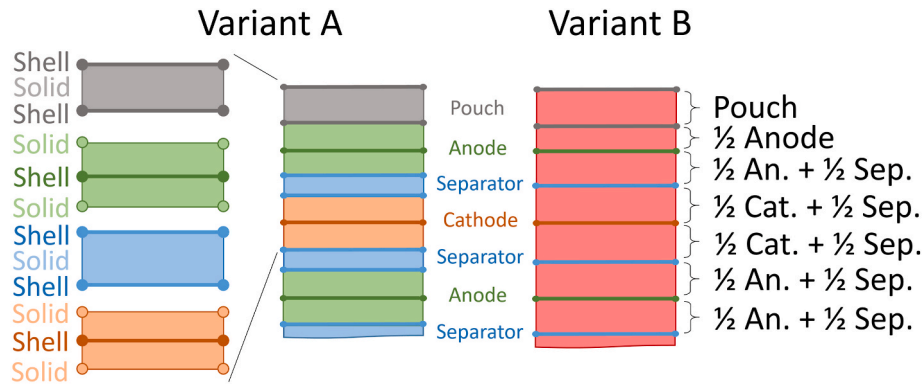


Fig. 1. Comparison of the two approaches (left: Variant A, right: Variant B).

$$\Delta t_e = \frac{2}{\omega_{max}} \quad (4)$$

$$\det(\mathbf{K} - \omega^2 \mathbf{M}) = 0 \rightarrow \omega_{max} \quad (5)$$

To create a realistic short-circuit criterion, the failure of the separator layers is simulated. This is inspired by the work of Yuan et al., who show that a short-circuit can be predicted from the strain state of the separator [43]. This avoids the use of auxiliary variables and allows an internal short-circuit to be derived from the simulated mechanical failure of the separators.

### 2.2.1. In-plane behaviour

The in-plane behaviour of all four components (anode, cathode, separator and pouch) is covered by shell elements. Assuming that the electrodes do not exhibit significant anisotropic behaviour, an isotropic material model is used. Similarly, the pouch layer, which features an aluminium core just like the cathode is modelled isotropic. An elastic-plastic material model (\*MAT\_PIECEWISE\_LINEAR\_PLASTICITY) is used for these three components. With \*MAT\_ADD\_EROSION, a maximum principal strain failure criterion is applied.

The anisotropic material model \*MAT\_EXTENDED\_3-PARAMETER\_BARLAT is used for modelling the separator. With the extended version of the original model, the yield stress depends on the material direction and loading state [45]. The anisotropic plasticity is specified by three independent load tables (stress vs. strain and strain rate).

Due to the anisotropy in mechanical behaviour, selecting an isotropic failure model is not expedient. In this case, an orthotropic failure model is implemented through \*MAT\_ADD\_GENERALIZED\_DAMAGE, which offers the possibility to define damage initiation, failure strain and damage accumulation over strain and triaxiality  $\eta$  (ratio between hydrostatic stress  $\sigma_H$  and von Mises stress  $\sigma_M$ ). As shown in Equation (6), the damage tensor contains three main damage coefficients  $D_i$ . These are each a function of the exponent for damage-related stress fadeout  $FADEXP_i$  and the damage threshold value (critical damage)  $DCRIT_i$  or critical history value (material instability)  $ECRIT_i$  depending on the triaxiality. The resulting damage tensor represents the relationship between the undamaged stresses  $\tilde{\sigma}_{ij}$  and damaged stresses  $\sigma_{ij}$ . [46]

$$\begin{bmatrix} \sigma_{11} \\ \sigma_{22} \\ \sigma_{33} \\ \sigma_{12} \\ \sigma_{23} \\ \sigma_{31} \end{bmatrix} = \begin{bmatrix} (1 - D_1) & 0 & 0 & 0 & 0 & 0 \\ 0 & (1 - D_2) & 0 & 0 & 0 & 0 \\ 0 & 0 & 1 & 0 & 0 & 0 \\ 0 & 0 & 0 & (1 - D_3) & 0 & 0 \\ 0 & 0 & 0 & 0 & 1 & 0 \\ 0 & 0 & 0 & 0 & 0 & 1 \end{bmatrix} \begin{bmatrix} \tilde{\sigma}_{11} \\ \tilde{\sigma}_{22} \\ \tilde{\sigma}_{33} \\ \tilde{\sigma}_{12} \\ \tilde{\sigma}_{23} \\ \tilde{\sigma}_{31} \end{bmatrix}$$

with

$$D_i \rightarrow \left( \frac{D_i - DCRIT_i}{1 - DCRIT_i} \right)^{FADEXP_i} \quad (6)$$

The damage is driven by the history variable  $HIS_i$  and its time derivative. The course of all defined damage coefficients can be determined individually via the parameter  $DMGEXP_i$ . (Equation (7)) The failure strains  $\epsilon_{f,i}$  can also be defined independently of each other as a function of triaxiality  $\eta$ . Both failure strain  $\epsilon_{f,i}$  and critical history value  $ECRIT_i$  are defined by a table of triaxiality and strain rate. [46]

$$\dot{D}_i = DMGEXP_i \bullet D_i \left( 1 - \frac{1}{DMGEXP_i} \right) \bullet \frac{HIS_i}{\epsilon_{f,i}} \quad (7)$$

When one of the three damage coefficients reaches the value 1 (complete damage), the corresponding element erodes. In this way, separator failure is represented in detail. The internal short-circuit is determined by analysing the eroded energy of all separator layers. As shown in Equation (8), a hard short-circuit occurs when the eroded energy  $E_{eroded}^{Separator}$  is greater than zero. The critical position can be determined by analysing the fringe plot.

$$Hard\ ISC = \begin{cases} true & \text{if } E_{eroded}^{Separator} > 0 \\ false & \text{else} \end{cases} \quad (8)$$

### 2.2.2. Out-of-plane behaviour

The out-of-plane behaviour is entirely generated by the solid elements, located between the shell element layers. With variant B, the transverse compression behaviour is homogenised (i.e., each layer is assigned an identical transverse compression response behaviour). In variant A, each layer has transverse compression response behaviour. Regardless of the variant, the \*MAT\_MODIFIED\_HONEYCOMB material model is used for the solids in both cases. This is a decoupled material model. It allows the mechanical behaviour of all six directions to be defined independently. A discrete element formulation is possible, especially for this material model. Thus, compression of the already thin elements does not lead to time-step drops. Additionally, when selecting a nodal-mass based time-step calculation, higher time-steps for the light and thin separator will be achieved, due to shared nodes. The solids must not show any mechanical response under in-plane loads, as this is covered by the shell elements. Thus, the mechanical behaviour in the u- and v-directions remain undefined. The same applies to the uv-shear component. Thus, only the behaviour in the thickness direction (w-direction) and the out-of-plane shear behaviour remain to be defined for the solid elements. In other words, the layers behave like cohesive elements but with the main difference that non-linear compression behaviour can be realised, which is crucial when depicting transverse compression behaviour. However, unlike with tie-shell elements (element formulation 20 in LS-DYNA), moments are not transferred. This appears to be a reasonable assumption, given the minimal distance between the adjacent shell elements and the small thickness of the current collectors that are spuriously bridged by the solid elements.

No failure modelling in element erosion is considered for transverse compression (failure will only occur if the underlying shells erode).

### 2.2.3. Morphological modelling

A cell has special areas besides the jelly stack, which must be considered separately. The cell tabs are the cell parts that connect the individual anode or cathode layers and lead out of the pouch, forming the terminals there. On the opposite side of the cell, all the separator layers are connected to hold them in place by pressing them onto the edge of the envelope [44].

Fig. 2a and b shows the modelling approach of the mentioned areas. The cell tabs are modelled by shell elements. The same principle is used to model both the connection of the separators and the pouch fold. (Fig. 2c)

A mesh size of  $2.5 \times 2.5$  mm was chosen for the discretisation. This was considered sufficiently small for the load cases under study in this work. For other load cases, such as in-plane loads or highly localised indentations, a smaller mesh size is recommended. This discretisation affects all layers to allow for a connection by shared nodes between the shell and solid elements.

The thicknesses of the individual layers (compare Table 1) do not add up to the thickness of the real cell. This is likely caused by the disassembly of the cell into its components. During dissection, the cell is discharged, and the electrolyte evaporates. The thickness of the individual layers is therefore reduced by 2.5–2.8% to match the thickness of the real cell. This resulted in the following values for the individual components:

- separator 19.5  $\mu\text{m}$ ,
- anode 136  $\mu\text{m}$ ,
- cathode 165.2  $\mu\text{m}$
- and pouch 184.9  $\mu\text{m}$ .

The electrolyte is assumed to be almost incompressible. Under volumetric loading, its behaviour contributes considerably to mechanical behaviour. In this model approach, an airbag model of a linear fluid represents the electrolyte. This is mainly to replicate the cell behaviour under volumetric loading. In LS-DYNA, the airbag model \*AIRBAG\_LINEAR\_FLUID is used. As shown in Equation (9), the pressure  $p$  depends on the bulk modulus  $K$  and the ratio of the control volume  $V_0$  to the compressed volume  $V$ .

$$p = K \ln\left(\frac{V_0}{V}\right) \quad (9)$$

For the parameter  $V_0$  the entire volume of the pouch is used. (Fig. 2c) The bulk modulus  $K$  was set to a constant 1.8 GPa, which should represent an approximately incompressible fluid. This approach is suitable for considering the electrolyte under quasi-static loading. For dynamic loading, the influence of the electrolyte on the mechanical behaviour would also have to be taken into account, as presented by Kisters et al. [47].

### 2.3. Experiments

#### 2.3.1. In-plane behaviour – characterisation

Tensile tests of the individual components were conducted to calibrate the material models of the shell elements. The cell was discharged to a state of charge (SOC) of 0% for safety reasons before disassembly. Test specimens 5 mm wide and 15 mm long at three orientations ( $0^\circ$  and  $90^\circ$  relative to the u-axis) were extracted (cut out) out of the individual layers of the anode and cathode. For the separator and pouch, additional samples for the diagonal direction ( $45^\circ$  relative to the u-axis) were cut out. Specimens were tested at two loading rates: 20 mm/min and 600 mm/min.

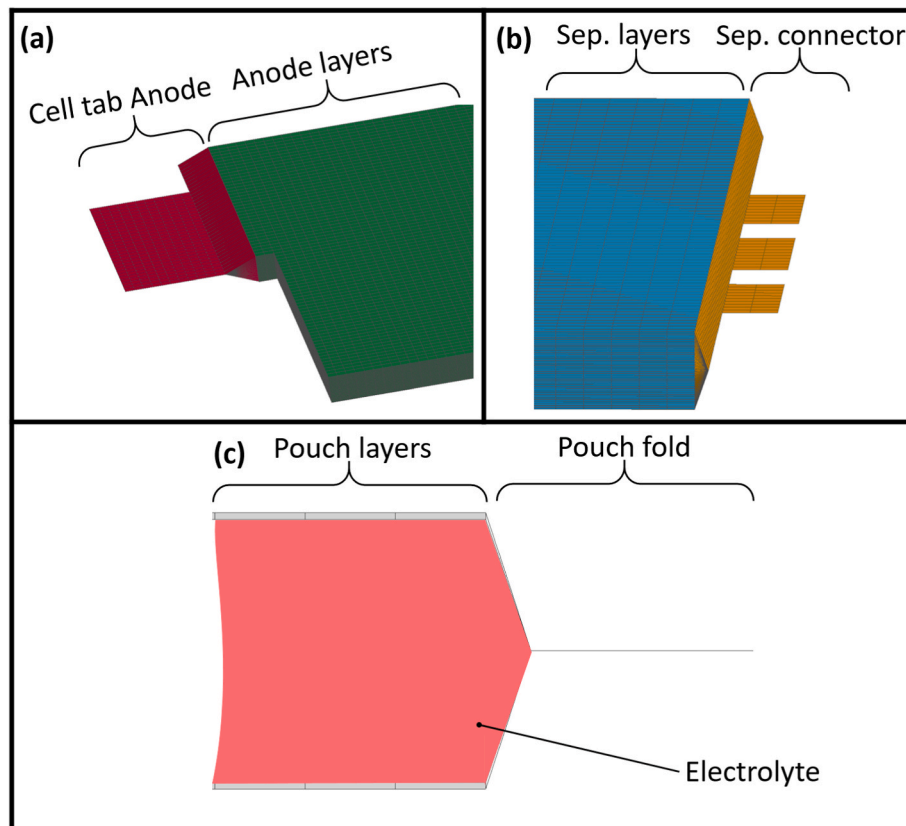


Fig. 2. Modelling approaches a) Cell tab b) Separator connector c) Pouch fold and electrolyte.

### 2.3.2. Out-of-plane behaviour – characterisation and calibration

For the behaviour in the thickness direction in variant A, the results of compression tests of the components are used for characterisation. The components anode, cathode and separator are examined regarding their transverse pressure properties by joining multiple identical layers to form a stack until the desired height of approximately 1 mm is reached. This was done to minimise possible measurement errors regarding displacement. For the anode and cathode, seven layers were each used. A total of 47 layers formed a stack for the separator. To exclude the influence of stacking errors (exact positioning of layers on top of each other), the samples were made larger than the impactor. The sample stacks were loaded with a flat end cylinder (diameter 11 mm) at two loading rates (1 mm/min and 10 mm/min). (Fig. 3)

The samples were soaked in a substitute electrolyte (propylene carbonate) to test the components as realistically as possible. For the characterisation of the pouch under transverse compression, a 3-mm diameter impactor loads a single layer. This is because, considering the thickness, only two layers occur in the cell, and these are not saturated with electrolytes.

For variant B, the solids represent homogenised behaviour in the w-direction. Therefore, the results of the cell tests are used for calibration. Hence, an indentation test across the short side with a cylindrical impactor ( $D = 30$  mm) was used (Fig. 4b).

Both variants are calibrated in terms of out-of-plane shear against, the results of a 3-point bending test. (Fig. 4d)

### 2.3.3. Cell tests for calibration and validation

Besides the cell tests for transversal compressive behaviour, which is the focus of this work, other tests were performed to calibrate the interlaminar shear. Consistently with the material characterisation tests, cell tests were performed at SOC 0%.

The first test configuration is the penetration test with a cylindrical impactor of 30 mm in diameter with its axis parallel to the u-axis (Fig. 4a). In this case, the cylinder penetrates the centre of the cell over its entire length. The same test over the short side (the cylindrical axis parallel to the v-axis, Fig. 4b). Local differences in the transverse compression behaviour can be observed, which may be caused, for example, by the cell tabs, separator connector or anisotropy of the separator layers.

In a third configuration (Fig. 4c), the cell is penetrated by a hemispherical impactor. As the contact area is much smaller than that of the cylindrical impactor, stiffness is lower as compared to first and second configuration.

In the fourth configuration (Fig. 4d) the cell is exposed to 3-point bending with a cylindrical impactor and cylindrical supports, each 30 mm in diameter. The span-width was 120 mm. As an experimental aid, a steel plate (DC01) with a thickness of 1 mm is positioned between the cell and the supports.

Each test was conducted quasi-statically (1 mm/s). During the tests, the electrical voltage of the cell was recorded in addition to the penetration force of the impactor and its displacement. The voltage drop is considered an indicator of the internal short-circuit. This approach is well known in literature ([12,22,25]). As the component tests and the

cell experiments were performed at the same SOC, the drop in cell voltage can be used as a validation variable for separator failure. For the different test configurations, five repetitions were carried out for statistical validation.

All these tests were simulated to calibrate and validate the models.

## 3. Results

### 3.1. In-plane behaviour

Fig. 5a shows the results of the tensile tests for the components anode, cathode and pouch. Strain rate and loading direction showed little to no effect on the component behaviour. Therefore, curves were averaged over all ( $n = 12$  for anode and cathode –  $n = 18$  for pouch) single measurements. These were used as a target for the material modelling. On average, the anode samples failed at a strain of 3.1% ( $\pm 1.0\%$ ), the cathode samples at 1% ( $\pm 0.22\%$ ) and the pouch material at around 65% ( $\pm 18\%$ ). Fig. 5b shows the curves for the separator samples, with distinct anisotropic and strain-rate dependent mechanical behaviour. Least strain rate effects were observed in the u-direction. The orthotropic failure model is calibrated against the failure strains of the tensile tests can be used to calibrate the failure model. As suitable test configurations for shear ( $\eta = 0$ ) and in-plane compression ( $\eta = -\frac{1}{3}$ ) are lacking, the values for uniaxial tension ( $\eta = \frac{1}{3}$ ) are used for these ranges. Compared to the measured curves, the simulation curves of all tensile tests show that all essential mechanical characteristics can be represented. The determined material parameters used for modelling are listed in Table 2. Young's moduli were determined by simulating individual tensile tests. The Poisson's ratios of copper and aluminium were assumed for the electrodes and the pouch.

### 3.2. Out-of-plane behaviour

Fig. 6 visualises the test and simulation results of the compression tests. Notably, the pouch compression tests are based on a single layer, while the others were multi-layer compression tests. The penetration of the impactor with rounding leads to an inhomogeneous stress state. Therefore, a force-displacement curve was used to calibrate the material models. The results show that the loading rate significantly influences the transverse compression behaviour of the separator compared to the anode, cathode and pouch. For the latter components, the target curves can be safely averaged over all test specimens ( $n = 3$ ) and loading rates ( $m = 2$ ). With the separator, the average curves are established for each loading rate independently.

The simulations for the anode, cathode and pouch fit the target curves well. The simulation results of the separator tests exhibit deviations. This can be attributed to the comparatively simple strain rate model of \*MAT\_MODIFIED\_HONEYCOMB, where the yield curve is scaled based on the compression rate.

The presented results of the tensile tests are incorporated into the cell model of variants A and B by adapting the respective material models for the shell elements. The compression tests, however, were only integrated in variant A, as the behaviour of transverse compression in variant B is not based on the individual components but on the results of the entire cell.

### 3.3. Cell behaviour and short-circuit prediction

The results of the cell tests and their simulations are shown in Fig. 7. The different diagrams show the measured and simulated impactor force over penetration; the measured cell voltage is also shown. The voltage drop is assumed to coincide with the failure of the separator. The maximum and minimum envelopes are shown in solid grey lines. Fig. 7a–c compares the experiment and simulation of the indentation tests with the configurations in Fig. 4a–c. Both variants A and B are

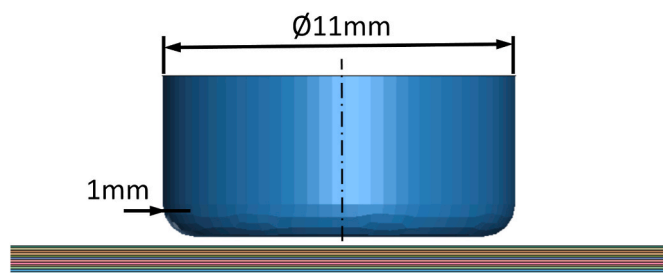


Fig. 3. Exemplary illustration of the compression test.

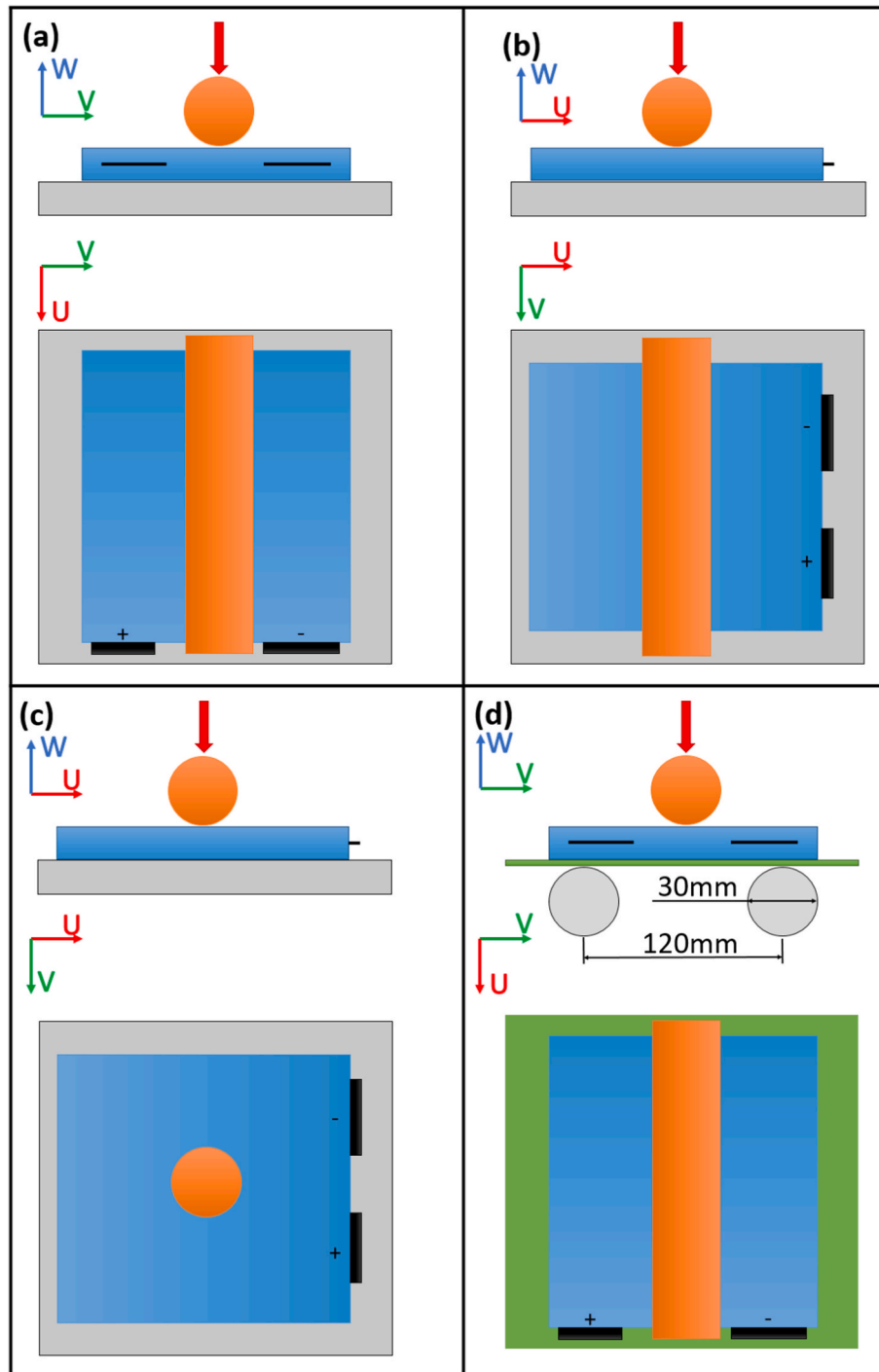


Fig. 4. Cell test configurations a) Indentation test with cylindrical impactor long side b) Indentation test with cylindrical impactor short side c) Indentation test with hemispherical impactor d) 3-point bending test.

shown side by side (green and blue solid lines). The vertical red lines mark the point where the first separator elements erode, indicating an internal short-circuit. This point is determined by analysing the eroded energy of all separator layers, as described in Equation (8). The location of failure is detected by the use of the fringe plot. This is schematically shown for the indentation test short side in Fig. 7e. In the section, only the separator layers are visible. The upper layer is coloured red, while all others are blue. Here, it is clearly visible where the elements erode. The diagram below shows the course of the eroded energy of all separators over the displacement. This clearly shows the intrusion at which a hard internal short-circuit occurs. The maximum relative deviation of the

simulated separator failure from the measured internal short-circuit is around 10%. In addition, the effective stress (von Mises) is shown over the cross-section of the cell at an intrusion of 2.5 mm. This shows an essential advantage of the hybrid modelling approach of shells and solids. Although shell elements have already been eroded, the stability of the cell model is maintained by the solid elements.

For the characterisation of the behaviour in the thickness direction of variant B, the results of the cell test with a cylindrical impactor (Fig. 4b) are used. The simulation results show that the negative effects of this simplification on the level of fidelity are limited. Additionally, an increase in the initial time step to 1.33E-05 ms was observed. This

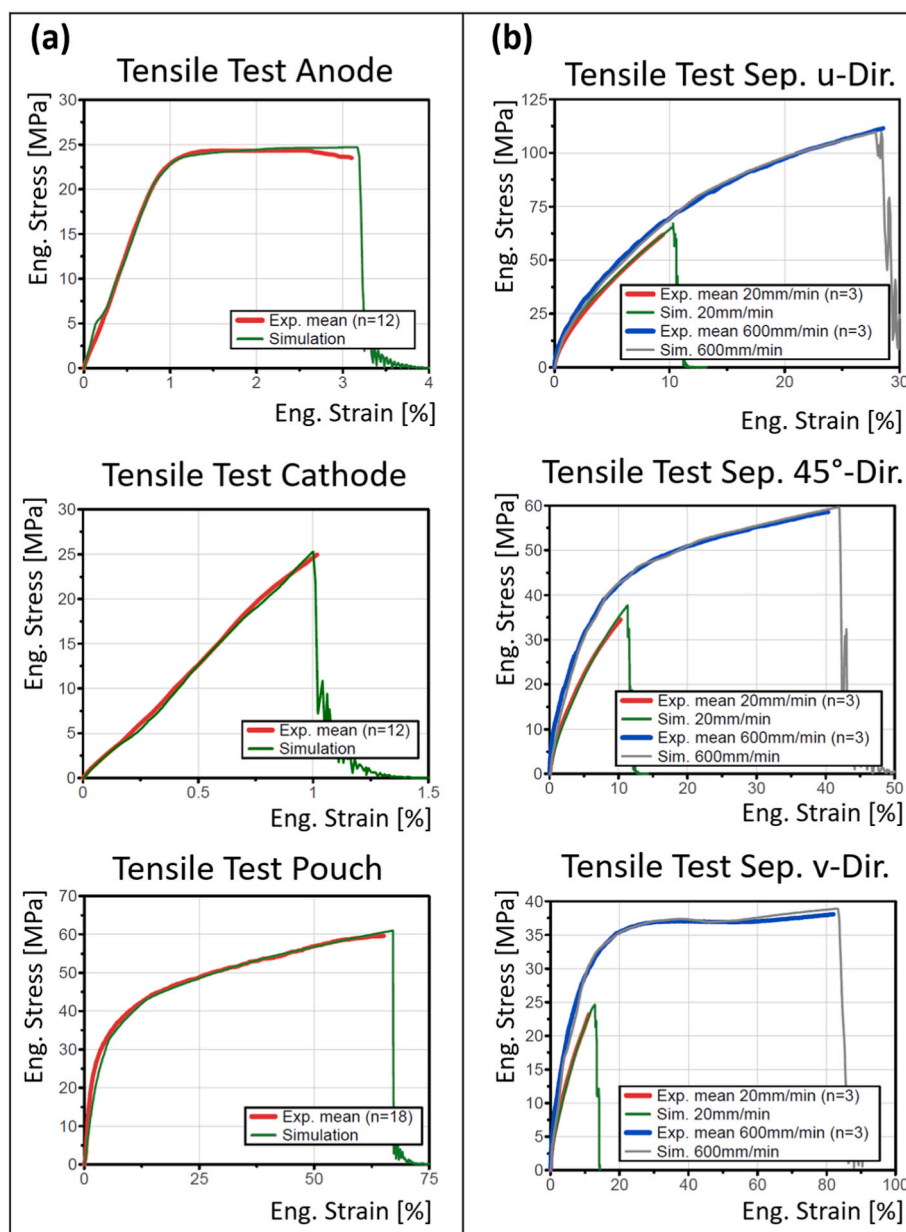


Fig. 5. Comparison between simulation and real component tests a) Tensile test anode, cathode and pouch b) Tensile test separator.

Table 2  
In-plane parameters of components.

Components	Parameter		
	Young's Modulus E [GPa]	Poisson's Ratio $\nu$ [-]	Failure Strain $\epsilon_f$ [%]
Anode	3.0	0.35	3.1
Cathode	2.5	0.35	1.0
Separator	1.15	0.01	9.1–82.0
Pouch	1.75	0.35	65.0

represents a relative improvement of 48%.

However, it is evident that the simulation curve drops in comparison to the experiment. This is due to the premature failure of the cell. The failure point coincides with the beginning of the force drop.

Fig. 7d shows the results of the 3-point bending test. As the impactor displacement is much greater than in the other test configurations, this is

simulated exclusively with variant B over a displacement of 25 mm. A simulation with variant A is inappropriate due to increased computational effort. As can be seen from this illustration, no cell failure occurred during the bending load. The simulation results show that the initial slope hit very well, but the simulation curve went slightly above the plateau.

Approximately 40% more elements are required for modelling the cell with variant A than with variant B. In addition, a larger time step can be achieved with variant B. Both aspects result in the calculation time of variant B being halved compared to variant A.

Fig. 8 compares the behaviour in the thickness direction of both variants. Here, the RVE of the jelly stack was subjected to transverse compression. This clearly shows that variant B is a simplification. The components were compressed unevenly, which was already to be expected from the compression tests of the components. (Compare Fig. 6)

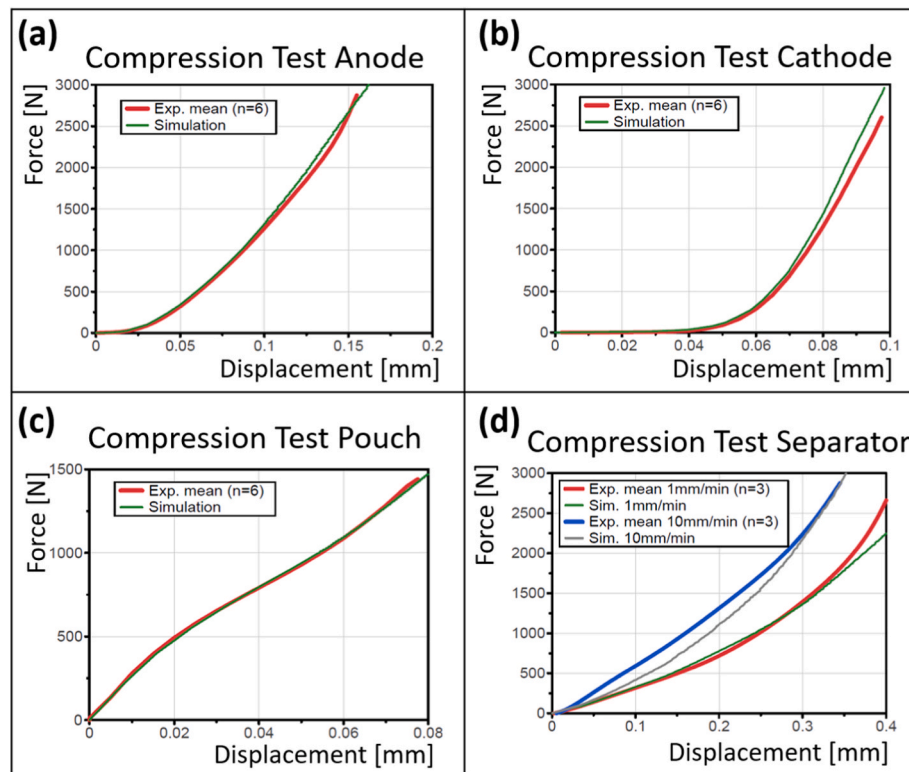


Fig. 6. Comparison between simulation and real compression test a) anode b) cathode c) pouch d) separator.

#### 4. Limitations

The failure of the separator layers is used as a short-circuit criterion. However, this is only the case for a so-called hard ISC. An adaptation of the criterion would be required to detect soft ISC (flattening of the separator).

A mesh size of  $2.5 \times 2.5$  mm was chosen as the in-plane discretisation for both variants. The subdivision of the components in the thickness direction for variant A resulted in the solid elements of the separator having large aspect ratios. This was considered sufficiently small, as this work focuses on transverse loads. For other load cases, such as in-plane crush or localised indentations, an adjustment of the mesh size is recommended. This, of course, results in increased computational effort.

The modelling methods presented in this study were used on a cell with a SOC of 0%. If a more comprehensive model with a higher SOC is desired, one would need to consider either taking components from charged cells, since Sonwane et al. showed the dependence of mechanical properties on SOC [48]. As this is difficult from a safety viewpoint, macroscopic modelling of SOC dependence is being considered. However, this work is limited to the modelling of a cell with a SOC of 0%. In addition, the modelling approaches were adjusted to the quasi-static behaviour of the cell. Accordingly, it is assumed that there is no change in the stiffness of the cell due to dynamic effects of the electrolyte.

#### 5. Conclusion

The scope of this work was to develop a finite element model of a lithium-ion pouch cell that combines high level of detail and relatively high computational efficiency. Therefore, the use of penalty contacts within the jelly stack was completely omitted. Furthermore, a discrete element formulation is applied, which successfully prevents a reduction in the time step under transverse compression. Two modelling approaches, denoted as variants A and B, were investigated. The key properties of both variants are shown in Table 3.

In variant A, the transverse compression behaviour of individual layers is considered, while in variant B, transverse compression behaviour is homogenised over the thickness.

For both variants, the geometric properties are modelled in detail, such as cell tabs and pouch envelope. For the characterisation of in-plane behaviour, component tests are required for both variants. The behaviour in the thickness direction is based on data from component tests only for variant A. Cell tests are required for variant B. The inter-laminar behaviour was calibrated against 3-point bending tests for both variants. Eventually, the cell was validated against various transverse compression experiments.

Both variants performed quite similarly in overall structural response. The short-circuit criterion matches well with the drop in cell voltage in the experiments (max. deviation of 10%). However, an extension of this criterion is necessary to predict soft ISC (separator flattening). Similar to the work of Li et al. [31] and Jia et al. [27], this could be done through data-driven security risk prediction. In addition, a post-mortem analysis of the cells would be of great interest. This would allow the failure model to be validated on a component basis. However, as reactions in the cell occurs after the short-circuit despite a SOC of 0%, an analysis of the structure is not expedient. This has the potential for improvement and should be implemented in future work.

Despite the efficient modelling due to the points mentioned, the computational effort is extremely high in absolute terms, even for the more efficient variant B. In addition, the critical time step is too small by at least a factor of 10 to combine this model with common vehicle structure models without any problems. However, the main advantages of these approaches are their transferability and high level of detail. Despite the simplifications, the separator's failure can be simulated and thus the cell failure can be predicted. An adaptation of the model to a new cell type is already possible with knowledge of the geometry and mechanical properties of the new components. The effort for renewed characterisation tests, which would be necessary for adapting homogeneous models, can be significantly reduced here. A further reduction of computational effort would be conceivable in the future through the

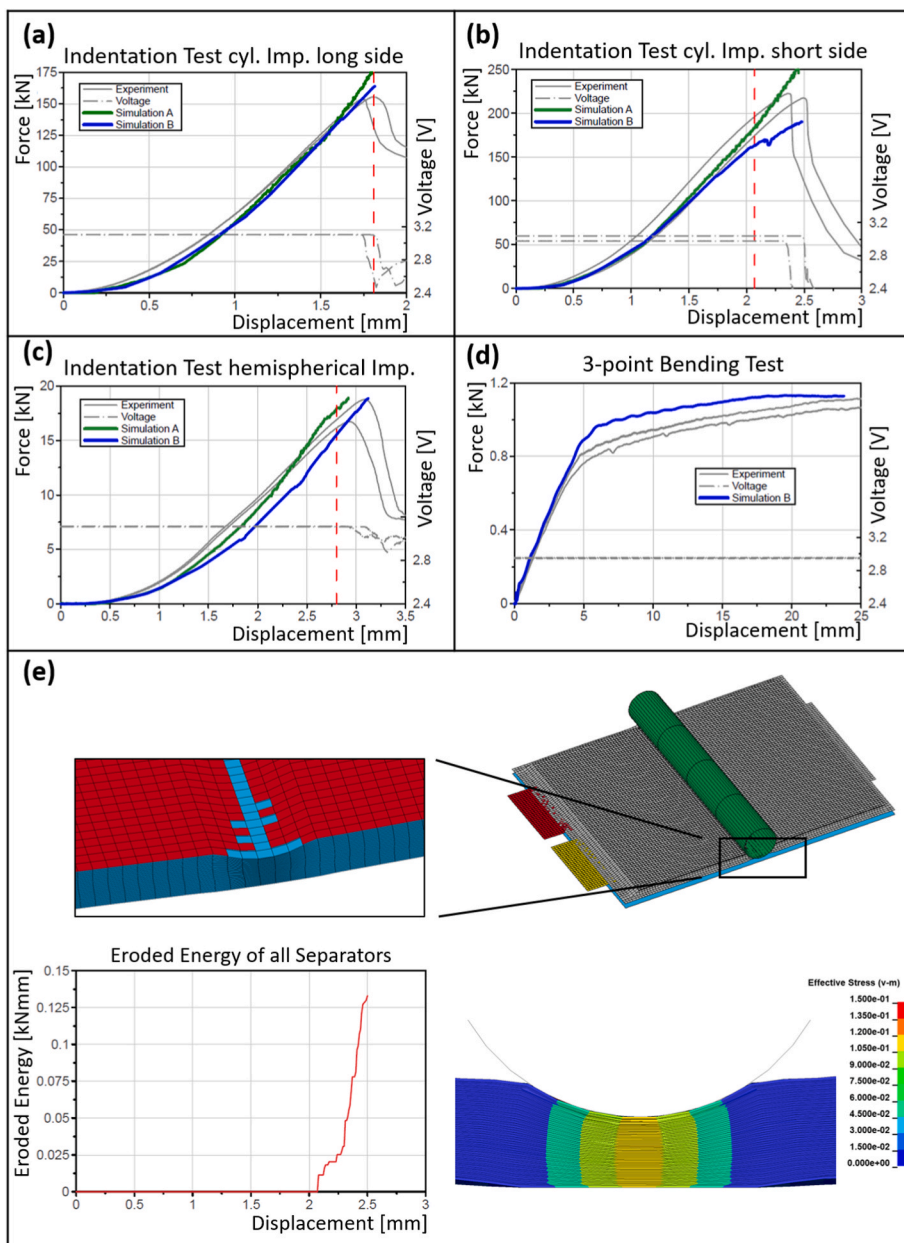


Fig. 7. Comparison between simulation and real cell tests a) Indentation test with cylindrical impactor long side b) Indentation test with cylindrical impactor short side c) Indentation test with hemispherical impactor d) 3-point bending test e) Schematic failure analysis.

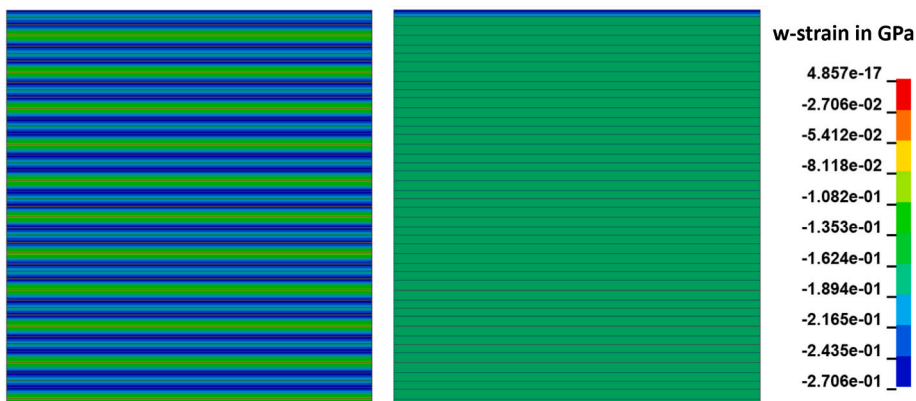


Fig. 8. Comparison of w-strain over thickness with transversal compression left) Variant A right) Variant B.

Table 3

Comparison of the key properties of both variants.

Property	Variant A	Variant B
Number of nodes	2 916 165	2 191 089
Number of elements	1 907 809	1 325 192
Initial time step [ms]	8.96E-6	1.33E-5
Characterisation	In-plane behaviour	Component tests
	Transversal behaviour	Component tests
	Bending behaviour	Cell tests

application of model order reduction [49] or multi-scale approaches.

### CRedit authorship contribution statement

**Alexander Schmid:** Data curation, Conceptualization, Methodology, Visualization, Writing – original draft, Writing – review & editing. **Christian Ellersdorfer:** Conceptualization, Methodology, Writing – review & editing, Supervision, Project administration. **Marco Raffler:** Data curation, Conceptualization, Methodology, Validation, Writing – review & editing, Supervision. **Nils Karajan:** Writing – review & editing. **Florian Feist:** Conceptualization, Methodology, Writing – review & editing, Supervision.

### Declaration of competing interest

The authors declare that they have no known competing financial interests or personal relationships that could have appeared to influence the work reported in this paper.

### Data availability

The authors do not have permission to share data.

### Acknowledgement

The authors would like to acknowledge the use of HPC resources provided by the ZID of Graz University of Technology.

This work was conducted during the realisation of the project Safe-Battery and its follow up SafeLIB (Grant agreement No. 882506) at Vehicle Safety Institute of Graz University of Technology.

SafeBattery was funded within the Province of Styria, as well as the Styrian Business Promotion Agency SFG.

The follow up SafeLIB has additionally been funded by the Province of Upper Austria.

Both projects are administered by the Austrian Research Promotion Agency (FFG).

The authors would like to thank the mentioned agencies and the cooperating companies.

In addition, the authors would like to thank the following persons: Clemens Dünser for providing valuable support throughout the Safe-Battery project and Wolfgang Sinz for his exceptional project management of SafeBattery and mentoring.

### References

- [1] C. Li, L. Liu, S. Lin, S. Liu, Research on fire fighting and emergency rescue of all-electric vehicle traffic accident, *J. Phys.: Conf. Ser.* 1972 (1) (2021), 12122, <https://doi.org/10.1088/1742-6596/1972/1/012122>.
- [2] M. Zwicker, M. Moghadam, W. Zhang, C.V. Nielsen, Automotive battery pack manufacturing – a review of battery to tab joining, *Journal of Advanced Joining Processes* 1 (2020), 100017, <https://doi.org/10.1016/j.jajp.2020.100017>.
- [3] C. Essl, A.W. Golubkov, A. Fuchs, Comparing different thermal runaway triggers for two automotive lithium-ion battery cell types, *J. Electrochem. Soc.* 167 (13) (2020), 130542, <https://doi.org/10.1149/1945-7111/abbe5a>.
- [4] E. Martínez-Rosas, R. Vasquez-Medrano, A. Flores-Tlacuahuac, Modeling and simulation of lithium-ion batteries, *Comput. Chem. Eng.* 35 (9) (2011) 1937–1948, <https://doi.org/10.1016/j.compchemeng.2011.05.007>.
- [5] S. Lee, S.S. Park, Atomistic simulation study of monoclinic Li<sub>3</sub>V<sub>2</sub>(PO<sub>4</sub>)<sub>3</sub> as a cathode material for lithium ion battery: structure, defect chemistry, lithium ion transport pathway, and dynamics, *J. Phys. Chem. C* 116 (48) (2012) 25190–25197, <https://doi.org/10.1021/jp306105g>.
- [6] Y. Long, et al., Molten lithium metal battery with Li<sub>4</sub>Ti<sub>5</sub>O<sub>12</sub> cathode and solid electrolyte, *eTransportation* 16 (2023), 100235, <https://doi.org/10.1016/j.etrans.2023.100235>.
- [7] M. Dubarry, N. Vuillaume, B.Y. Liaw, From single cell model to battery pack simulation for Li-ion batteries, *J. Power Sources* 186 (2) (2009) 500–507, <https://doi.org/10.1016/j.jpowsour.2008.10.051>.
- [8] Z. Wang, J. Ma, L. Zhang, Finite element thermal model and simulation for a cylindrical Li-ion battery, *IEEE Access* 5 (2017) 15372–15379, <https://doi.org/10.1109/ACCESS.2017.2723436>.
- [9] D.H. Jeon, S.M. Baek, Thermal modeling of cylindrical lithium ion battery during discharge cycle, *Energy Convers. Manag.* 52 (8–9) (2011) 2973–2981, <https://doi.org/10.1016/j.enconman.2011.04.013>.
- [10] S. Chen, et al., All-temperature area battery application mechanism, performance, and strategies, *Innovation* 4 (4) (2023), 100465, <https://doi.org/10.1016/j.xinn.2023.100465>.
- [11] C. Breiffuss, et al., A ‘microscopic’ structural mechanics FE model of a lithium-ion pouch cell for quasi-static load cases, *SAE Int. J. Passeng. Cars - Mech. Syst.* 6 (2) (2013) 1044–1054, <https://doi.org/10.4271/2013-01-1519>.
- [12] M. Raffler, A. Sevarin, C. Ellersdorfer, S.F. Heindl, C. Breiffuss, W. Sinz, Finite element model approach of a cylindrical lithium ion battery cell with a focus on minimization of the computational effort and short circuit prediction, *J. Power Sources* 360 (2017) 605–617, <https://doi.org/10.1016/j.jpowsour.2017.06.028>.
- [13] T. Wierzbicki, E. Sahraei, Homogenized mechanical properties for the jellyroll of cylindrical Lithium-ion cells, *J. Power Sources* 241 (2013) 467–476, <https://doi.org/10.1016/j.jpowsour.2013.04.135>.
- [14] J. Xu, B. Liu, L. Wang, S. Shang, Dynamic mechanical integrity of cylindrical lithium-ion battery cell upon crushing, *Eng. Fail. Anal.* 53 (2015) 97–110, <https://doi.org/10.1016/j.engfailanal.2015.03.025>.
- [15] E. Sahraei, E. Bosco, B. Dixon, B. Lai, Microscale failure mechanisms leading to internal short circuit in Li-ion batteries under complex loading scenarios, *J. Power Sources* 319 (2016) 56–65, <https://doi.org/10.1016/j.jpowsour.2016.04.005>.
- [16] S. Chen, et al., Mechanical strain signal based early warning for failure of different prismatic lithium-ion batteries, *J. Power Sources* 580 (2023), 233397, <https://doi.org/10.1016/j.jpowsour.2023.233397>.
- [17] B. Liu, et al., Safety issues and mechanisms of lithium-ion battery cell upon mechanical abusive loading: a review, *Energy Storage Mater.* 24 (2020) 85–112, <https://doi.org/10.1016/j.ensm.2019.06.036>.
- [18] F. Xiao, B. Xing, L. Kong, Y. Xia, Impedance-based diagnosis of internal mechanical damage for large-format lithium-ion batteries, *Energy* 230 (2021), 120855, <https://doi.org/10.1016/j.energy.2021.120855>.
- [19] D.P. Finegan, et al., The application of data-driven methods and physics-based learning for improving battery safety, *Joule* 5 (2) (2021) 316–329, <https://doi.org/10.1016/j.joule.2020.11.018>.
- [20] M. Zhou, L. Hu, S. Chen, X. Zhao, Different mechanical-electrochemical coupled failure mechanism and safety evaluation of lithium-ion pouch cells under dynamic and quasi-static mechanical abuse, *J. Power Sources* 497 (2021), 229897, <https://doi.org/10.1016/j.jpowsour.2021.229897>.
- [21] J. Kukreja, et al., Crash analysis of a conceptual electric vehicle with a damage tolerant battery pack, *Extreme Mechanics Letters* 9 (2016) 371–378, <https://doi.org/10.1016/j.eml.2016.05.004>.
- [22] L. Greve, C. Fehrenbach, Mechanical testing and macro-mechanical finite element simulation of the deformation, fracture, and short circuit initiation of cylindrical Lithium ion battery cells, *J. Power Sources* 214 (2012) 377–385, <https://doi.org/10.1016/j.jpowsour.2012.04.055>.
- [23] B. Dixon, A. Mason, E. Sahraei, Effects of electrolyte, loading rate and location of indentation on mechanical integrity of li-ion pouch cells, *J. Power Sources* 396 (2018) 412–420, <https://doi.org/10.1016/j.jpowsour.2018.06.042>.
- [24] R. Beaumont, I. Masters, A. Das, S. Lucas, A. Thanikachalam, D. Williams, Methodology for developing a macro finite element model of lithium-ion pouch cells for predicting mechanical behaviour under multiple loading conditions, *Energies* 14 (7) (2021) 1921, <https://doi.org/10.3390/en14071921>.
- [25] E. Sahraei, J. Campbell, T. Wierzbicki, Modeling and short circuit detection of 18650 Li-ion cells under mechanical abuse conditions, *J. Power Sources* 220 (2012) 360–372, <https://doi.org/10.1016/j.jpowsour.2012.07.057>.
- [26] A. Trondl, Sun Dong-Zhi, s. Sommer, Simplified modeling of pouch cells under different loadings, in: *13th European LS-DYNA Conference, 2021. Ulm, Germany*.
- [27] M.Y. Ali, W.-J. Lai, J. Pan, Computational models for simulations of lithium-ion battery cells under constrained compression tests, *J. Power Sources* 242 (2013) 325–340, <https://doi.org/10.1016/j.jpowsour.2013.05.022>.
- [28] P. Sonnberger, M. Behmer, E. Böhler, C. Breiffuss, A hybrid approach to derive macro- and meso-mechanic cell models for vibrational investigations of lithium-ion pouch cells, *J. Energy Storage* 49 (2022), 104060, <https://doi.org/10.1016/j.est.2022.104060>.
- [29] L. Tang, J. Zhang, P. Cheng, Homogenized modeling methodology for 18650 lithium-ion battery module under large deformation, *PLoS One* 12 (7) (2017), e0181882, <https://doi.org/10.1371/journal.pone.0181882>.
- [30] G. Kermani, M.M. Keshavarzi, E. Sahraei, Deformation of lithium-ion batteries under axial loading: analytical model and Representative Volume Element, *Energy Rep.* 7 (2021) 2849–2861, <https://doi.org/10.1016/j.egy.2021.05.015>.
- [31] B. Arief Budiman, S. Rahardian, A. Saputro, A. Hidayat, I. Pulung Nurprasatio, P. Sambegoro, Structural integrity of lithium-ion pouch battery subjected to three-

- point bending, *Eng. Fail. Anal.* 138 (2022), 106307, <https://doi.org/10.1016/j.engfailanal.2022.106307>.
- [32] Y. Jia, et al., Data-driven safety risk prediction of lithium-ion battery, *Adv. Energy Mater.* 11 (18) (2021), 2003868, <https://doi.org/10.1002/aenm.202003868>.
- [33] M. Gilaki, I. Avdeev, Impact modeling of cylindrical lithium-ion battery cells: a heterogeneous approach, *J. Power Sources* 328 (2016) 443–451, <https://doi.org/10.1016/j.jpowsour.2016.08.034>.
- [34] L. Wang, S. Yin, J. Xu, A detailed computational model for cylindrical lithium-ion batteries under mechanical loading: from cell deformation to short-circuit onset, *J. Power Sources* 413 (2019) 284–292, <https://doi.org/10.1016/j.jpowsour.2018.12.059>.
- [35] B. Schaufelberger, A. Altes, P. Matura, Modeling the mechanical behaviour of a Li-ion pouch cell under three-point bending, in: 13th European LS-DYNA Conference, 2021, Ulm, Germany.
- [36] W. Li, J. Zhu, Y. Xia, M.B. Gorji, T. Wierzbicki, Data-driven safety envelope of lithium-ion batteries for electric vehicles, *Joule* 3 (11) (2019) 2703–2715, <https://doi.org/10.1016/j.joule.2019.07.026>.
- [37] M. Plaimer, et al., Evaluating the trade-off between mechanical and electrochemical performance of separators for lithium-ion batteries: methodology and application, *J. Power Sources* 306 (2016) 702–710, <https://doi.org/10.1016/j.jpowsour.2015.12.047>.
- [38] S. Kalnaus, Y. Wang, J.A. Turner, Mechanical behavior and failure mechanisms of Li-ion battery separators, *J. Power Sources* 348 (2017) 255–263, <https://doi.org/10.1016/j.jpowsour.2017.03.003>.
- [39] J. Xu, L. Wang, J. Guan, S. Yin, Coupled effect of strain rate and solvent on dynamic mechanical behaviors of separators in lithium ion batteries, *Mater. Des.* 95 (2016) 319–328, <https://doi.org/10.1016/j.matdes.2016.01.082>.
- [40] M.F. Lagadec, R. Zahn, V. Wood, Designing polyolefin separators to minimize the impact of local compressive stresses on lithium ion battery performance, *J. Electrochem. Soc.* 165 (9) (2018) A1829–A1836, <https://doi.org/10.1149/2.0041809jes>.
- [41] M.F. Lagadec, R. Zahn, V. Wood, Characterization and performance evaluation of lithium-ion battery separators, *Nat. Energy* 4 (1) (2019) 16–25, <https://doi.org/10.1038/s41560-018-0295-9>.
- [42] K.-H. Yang, Basic finite element method and analysis as applied to injury biomechanics, *Basic Finite Element Method as Applied to Injury Biomechanics* (2018) 377–378.
- [43] C. Yuan, L. Wang, S. Yin, J. Xu, Generalized separator failure criteria for internal short circuit of lithium-ion battery, *J. Power Sources* 467 (2020), 228360, <https://doi.org/10.1016/j.jpowsour.2020.228360>.
- [44] Kovachev, et al., Analytical dissection of an automotive Li-ion pouch cell, *Batteries* 5 (4) (2019) 67, <https://doi.org/10.3390/batteries5040067>.
- [45] Livermore Software Technology (LST), LS-DYNA® Keyword User's Manual Volume II R13, 2021, pp. 338–362.
- [46] T. Erhart, P. Du Bois, Andreade Filipe, Short introduction of a new generalized damage model, in: 11th European LS-DYNA Conference, 2017, Salzburg, Austria.
- [47] T. Kisters, M. Gilaki, S. Nau, E. Sahraei, Modeling of dynamic mechanical response of Li-ion cells with homogenized electrolyte-solid interactions, *J. Energy Storage* 49 (2022), 104069, <https://doi.org/10.1016/j.est.2022.104069>.
- [48] A. Sonwane, C. Yuan, J. Xu, Coupling effect of state-of-charge and strain rate on the mechanical behavior of electrodes of 21700 lithium-ion battery, *Journal of Electrochemical Energy Conversion and Storage* 18 (2) (2021), <https://doi.org/10.1115/1.4049042>.
- [49] B. Bognet, F. Bordeu, F. Chinesta, A. Leygue, A. Poitou, Advanced simulation of models defined in plate geometries: 3D solutions with 2D computational complexity, *Comput. Methods Appl. Mech. Eng.* 201–204 (2012) 1–12, <https://doi.org/10.1016/j.cma.2011.08.025>.